J Electroceram (2006) 17:741–748
DOI 10.1007/s10832-006-7776-0

Oxygen permeation properties and surface modification of acceptor-doped $CeO_2/MnFe_2O_4$ composites

Hitoshi Takamura · Hiroshi Sugai · Masato Watanabe · Takehiro Kasahara · Atsunori Kamegawa · Masuo Okada

Received: 31 July 2005 / Revised: 8 January 2006 / Accepted: 15 February 2006

Abstract The preparation and oxygen permeation properties of the $(Ce_{0.8}Pr_{0.2})O_{2-\delta}$ − x vol% $MnFe_2O_4$ composites, where $x = 0$ to 35, have been investigated. The samples were prepared by the Pechini method. In the case of $Ce_{0.8}Pr_{0.2}O_{2-\delta}$, an oxygen flux density of 6 $\mu mol \cdot cm^{-2} \cdot s^{-1}$ (L = 0.0247 cm) and the maximum methane conversion of 50% were attained at 1000°C. Unlike composites consisting of Gd-doped CeO_2 and $MnFe_2O_4$, the oxygen permeability of the $(Ce_{0.8}Pr_{0.2})O_{2-\delta}$ − x vol% $MnFe_2O_4$ composites was almost constant regardless of the volume fraction of $MnFe_2O_4$; however, the optimum volume fraction of $MnFe_2O_4$ was determined to be 5 to 25 in the context of the chemical and mechanical stabilities under methane conversion atmosphere. In addition, the surface modification of the $(Ce_{0.8}Gd_{0.2})O_{2-\delta}$ − 15 vol% $MnFe_2O_4$ composite was performed by using the FePt nanoparticles. The catalyst loading of 2.8 mg/cm^2 on the both side of the 0.3 mm-thick $(Ce_{0.8}Gd_{0.2})O_{2-\delta}$ − 15vol% $MnFe_2O_4$ composite increased the oxygen flux density from 0.30 to 0.76 $\mu mol \cdot cm^{-2} \cdot s^{-1}$ in the case of He/air gradients; however, the effect seems to be reduced in the case of high oxygen flux density caused by a large pO_2 gradient. Moreover, the Langmuir-Blodgett film of the FePt nanoparticles were successfully prepared on the tape-cast $(Ce_{0.8}Gd_{0.2})O_{2-\delta}$ − 15vol% $MnFe_2O_4$ composite. Hydrophobic treatments for the surface of the composite were crucial to achieve high transfer ratio for the deposition of the LB film.

Keywords Oxygen permeable ceramics · Pr-doped ceria · Methane conversion · FePt nanoparticles · Langmuir-Blodgett film

H. Takamura (✉) · T. Kasahara · A. Kamegawa · M. Okada
Department of Materials Science, Graduate School of Engineering, Tohoku University, 6-6-02 Aramaki Aza Aoba, Sendai 980-8578, Japan
e-mail: takamura@material.tohoku.ac.jp

H. Takamura · H. Sugai · A. Kamegawa · M. Okada
CREST, Japan Science and Technology Agency, Japan

H. Sugai
Three-R Corporation, 4-10-3 Chuo, Sendai 980-0021, Japan

M. Watanabe
MHW Informatics, Inc., 406-33-3 Yagiyama-kasumicho, Sendai 982-0831, Japan

T. Kasahara
Graduate student, Tohoku University

1 Introduction

Mixed oxide-ion and electronic conductors have been widely studied for use as electrodes of solid oxide fuel cells and oxygen permeable membranes. The oxygen permeable membranes are of interest, in view of their promising applications, such as production of pure oxygen from air and hydrogen from hydrocarbons [1, 2]. To date, a number of oxygen permeable ceramics have been developed including perovskite-type oxides in ternary or quarternary systems consisting of rare-earth, alkaline-earth, and transition metals. $Ba_{0.5}Sr_{0.5}Co_{0.8}Fe_{0.2}O_{3-\delta}$ [3], $La_{0.7}Sr_{0.3}Ga_{0.6}Fe_{0.4}O_{3-\delta}$ [4], and $Pr_{0.7}Sr_{0.3}Fe_{0.8}Al_{0.2}O_{3-\delta}$ [5] are well known to exhibit a high oxygen flux density reaching to 8 $\mu mol \cdot cm^{-2} \cdot s^{-1}$ at elevated temperatures under methane conversion atmosphere. In addition to those, dual-phase-type mixed conductors comprising of ionic and electronic conductive phases have been developed [6, 7]. Among a number of composite-type mixed conductors, Gd or Sm-doped CeO_2 with 15vol% $MnFe_2O_4$ was found to show a high

oxygen flux density of 10 μmol·cm^{-2}·s^{-1} at 1000 °C under methane conversion atmosphere [8, 9]. From microstructural observations, the high oxygen permeation flux originating from the low volume fraction of secondary phase (15vol% $MnFe_2O_4$) was attributed to the formation of grain boundary phases with electronic conductivity [9].

As a novel member of acceptor-doped CeO_2/$MnFe_2O_4$ composites, in this paper, Pr-doped CeO_2 is selected as an ion-conductive matrix phase. Unlike Gd or Sm-doping, Pr-doping raises both ionic and electronic conductivities of CeO_2 [10]. This increase in mixed conductivity is favorable for oxygen permeable ceramics. Shuk and Greenblatt have proposed that $Ce_{1-x}Pr_xO_{2-\delta}$, where $x = 0$ to 0.5, can be good oxygen permeable ceramics based on conductivity and electromotive force measurements [11]. In addition, Fagg et al. have recently reported the oxygen permeation properties of $Ce_{1-x}Pr_xO_{2-\delta}$ under small pO_2 gradients, for example, 4.7×10^{-8} mol·cm^{-2}·s^{-1} for 1 mm-thick $Ce_{0.8}Pr_{0.2}O_{2-\delta}$ at 1000 °C [12]. However, the feasibility of use of $Ce_{1-x}Pr_xO_{2-\delta}$ under large pO_2 gradients such as methane conversion atmosphere remains unknown as well as the effect of addition of electronic conductive phases on oxygen permeation properties. Thus, the first purpose of this study is to prepare the Pr-doped CeO_2/$MnFe_2O_4$ composites and evaluate their oxygen permeation properties.

In addition to material development, to further improve the oxygen permeation flux, it is important to enhance surface exchange kinetics. For the Gd-doped CeO_2/$MnFe_2O_4$ composites, the oxygen flux density under large pO_2 gradients is limited by surface exchange kinetics, especially, in the case of membrane thickness less than 0.5 mm [9]. The limitation of oxygen flux density by surface exchange kinetics takes place not only for the composites, but also for the perovskite-type materials. To overcome this problem, a porous catalyst layer such as (La, Sr)$CoO_{3-\delta}$ and (La, Sr)$MnO_{3-\delta}$ oxides, has been applied to the air-side surface of membranes [4]. In this study, an FePt nanoparticle catalyst layer was deposited on the Gd-doped CeO_2/$MnFe_2O_4$ composite by using an evaporation technique, and the effect of the catalyst layer on the oxygen permeation properties was investigated. Moreover, to precisely control the structure of FePt nanoparticle catalyst layer, and to enlarge the region of surface modification, the Langmuir-Blodgett technique was applied.

2 Experimental details

2.1 $Ce_{0.8}Pr_{0.2}O_{2-\delta}$ /$MnFe_2O_4$ composites

The composites of $Ce_{0.8}Pr_{0.2}O_{2-\delta}$ − x vol% $MnFe_2O_4$ (CPO-xMFO; $0 \leq x \leq 35$) were prepared by the Pechini process [13, 14]. Raw materials used were nitrates serving as metal sources, and citric acid and ethylene glycol serving as chelating agents. After polymerizing, carbonizing, and calcination at 700°C, the resultant oxide powders were pressed into pellets and finally sintered. To attain high oxygen flux density for composite materials, it is crucial to keep small grain sizes since surface exchange reactions take place in the vicinity of triple-phase boundaries; at the same time, the samples need to have high relative density to eliminate a mechanical leakage. Therefore, sintering temperatures were optimized for each composition. Table 1 summarizes the firing conditions and relative density for CPO-xMFO. All the samples were fired in air. For $Ce_{0.8}Pr_{0.2}O_{2-\delta}$ without $MnFe_2O_4$, a higher sintering temperature of 1550 °C and longer time are required to obtain a dense specimen. The firing temperature was found to be reduced with increasing the volume fraction of $MnFe_2O_4$, suggesting that $MnFe_2O_4$ phase may work as a sintering agent as reported for Co_3O_4-added (Ce, Gd)$O_{2-\delta}$ [15]. The reforming catalysts used were 10 mass% Ni supported on $(Ce_{0.8}Pr_{0.2})O_{2-\delta}$ powders.

Table 1 Sintering conditions and relative density of $(Ce_{0.8}Pr_{0.2})O_{2-\delta}$ – x vol%$MnFe_2O_4$

Composition	Sintering temp. (°C)	Time (h)	density (g/cm^3)	Theor. density (g/cm^3)	Relative density (%)
$x = 0$	1550	5	6.93	7.10	97.5
$x = 1$	1500	2	6.49	7.08	91.6
$x = 3$	1400	2	6.70	7.05	95.2
$x = 5$	1300	2	6.60	7.01	94.2
$x = 10$	1300	2	6.52	6.91	94.3
$x = 15$	1300	2	6.39	6.82	93.7
$x = 20$	1300	2	6.52	6.72	96.9
$x = 25$	1300	2	6.42	6.63	96.8
$x = 30$	1300	2	5.74	6.53	87.8
$x = 35$	1300	2	5.39	6.44	83.7

2.2 FePt nanoparticles and Langmuir-Blodgett (LB) films

The colloidal solution of FePt intermetallicnanoparticles was prepared by means of a solution-phase chemical synthesis technique reported by Sun et al. [16]. Pt- acetylacetonate and Fe-pentacarbonyl were used as metal sources; oleic acid and oleyl amine were used as stabilizers. The solvent and reducing agent were dioctylether and 1, 2-hexadecanediol, respectively. After size-selective precipitation, the FePt nanoparticles were dispersed into hexane to be concentration of 4.7mg/ml. To form a catalyst layer, the colloidal solution of 300 μl was dropped onto the $Ce_{0.8}Gd_{0.2}O_{2-\delta}$ − 15vol% $MnFe_2O_4$ (CGO-15MFO) disk with dimensions of ϕ8 mm × 0.3 mm in thickness, and the solvent was evaporated at room temperature.

To fabricate a Langmuir-Blodgett film, a monolayer of the FePt nanoparticles was formed by spreading the colloidal solution of 100 μl onto pure water (subphase). π−A

isotherms were recorded at 15.5 °C. As a substrate, Si wafers and150 μm-thick CGO-15MFO membranes prepared by a tape-casting technique were used [17]. The CGO-15MFO substrates were treated in hot nitric acid at approximately 100°C followed by rinse with pure water to make hydrophilic surface; on the other hand, they were treated in acetone and ethanol under reflux followed by rinse with pure water and ozone oxidation to make surface hydrophobic. The LB films of FePt nanoparticles were then deposited on the substrates by using a Langmuir trough. The structure and morphology of LB films were confirmed by means of X-ray diffraction and a scanning electron microscopy, respectively.

2.3 Oxygen permeation properties

The setup for oxygen permeation and methane conversion tests was described elsewhere [5]. The samples were subjected to various pO_2 gradients between air and either He, Ar-5%H_2, or Ar-10%CH_4 within the temperature range of 800 to 1000°C. Sweep gases were fed at a rate of 20 to 100 sccm. Gas concentration was determined by use of a gas chromatograph and a mass spectrometer. For methane conversion tests, Ar-5%H_2 gas was swept to activate the Ni-based reforming catalyst prior to Ar-10%CH_4 gas flow.

3 Results and discussion

3.1 $Ce_{0.8}Pr_{0.2}O_{2-\delta}/MnFe_2O_4$ composites

Phase identification was performed for CPO − x vol% MFO, where $0 \leq x \leq 35$. From XRD analyses, the composites with $x = 3$ or higher were found to comprise of (Ce, Pr)$O_{2-\delta}$ and $MnFe_2O_4$ phases. In addition, a small amount of $PrFeO_3$ was observed for $x = 10$ or higher. These phases present in CPO-xMFO were same as those in CGO-xMFO [8, 9]. With respect to the stability of $MnFe_2O_4$, Yoo and Tuller have reported the equilibrium phase stability diagram as functions of temperature and pO_2 as shown in Fig. 2 [18]. In which, the upper and lower boundaries of $MnFe_2O_4$ single phase region are given as a function of temperature as follows:

$$\log pO_2 \text{ (upper boundary)} = (11.7 \pm 0.6) - (1.87 \pm 0.08) \times 10^4/T \quad (1)$$

$$\log pO_2 \text{ (lower boundary)} = (22.3 \pm 2.3) - (4.2 \pm 0.3) \times 10^4/T \quad (2)$$

Based on the phase stability diagram, $MnFe_2O_4$ is stable under air at temperatures above approximately 1240°C; however, it partially decomposes into Fe_2O_3 (hematite) under air at temperatures less than 1240°C. The phase stability of

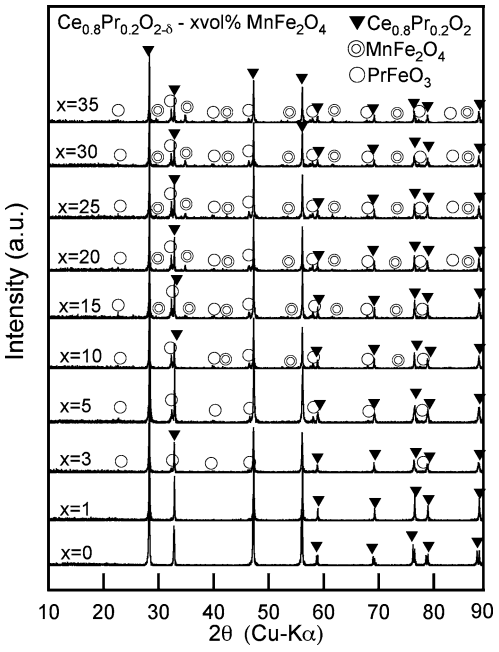

Fig. 1 X-ray diffraction patterns of of $Ce_{0.8}Pr_{0.2}O_{2-\delta}$ − x vol% $MnFe_2O_4$

$MnFe_2O_4$ has been also reported by Bonsdorf et al. [19]. This instability of $MnFe_2O_4$ under air may result in the formation of $PrFeO_3$ phase. In fact, no perovskite-type phase can be confirmed in the case of composites comprising of (Ce, Gd)$O_{2-\delta}$ and $CoFe_2O_4$ that is stable under air at wide temperature range but cannot be used for methane conversion purposes.

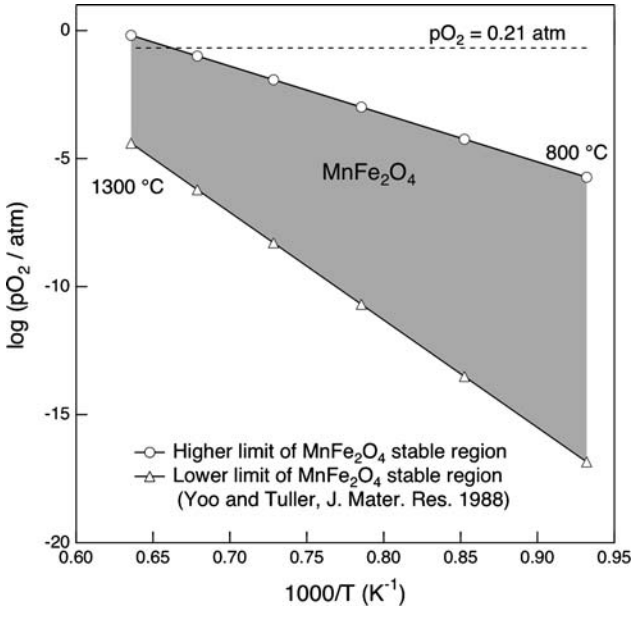

Fig. 2 The equilibrium phase stability diagram for $MnFe_2O_4$ as functions of temperature and pO_2 [18]

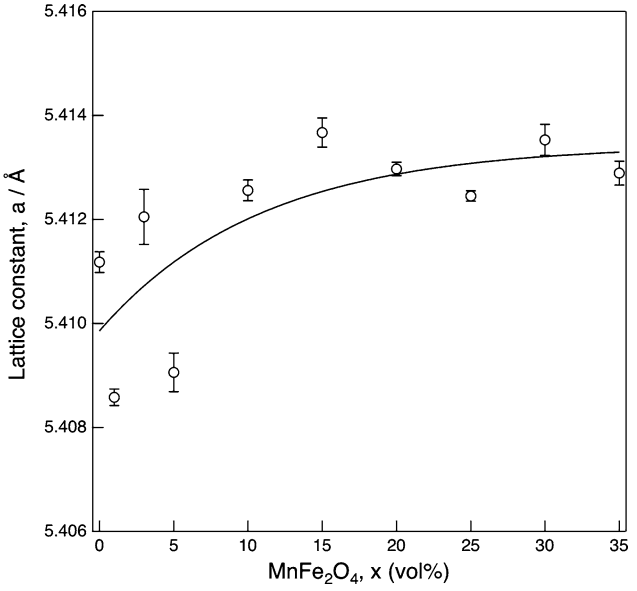

Fig. 3 The lattice constants of fluorite-type phase in $Ce_{0.8}Pr_{0.2}O_{2-\delta}$ − x vol% $MnFe_2O_4$

The lattice constant of the fluorite-type phase in the composites was calculated from the XRD patterns and was plotted in Fig. 3 as a function of the volume fraction of $MnFe_2O_4$. The lattice constant of the fluorite-type phase appears to increase with increasing x, even though data points are scattered especially at lower x values. As reported in Refs [20–22], the valence state of Pr and Ce cations, in other words, the lattice constant of (Ce, Pr)$O_{2-\delta}$ strongly depends on the history of the sample; for example, the lattice constant increases with increasing Pr content when a sample is quenched from 850°C; however, it decreases when a sample is slowly cooled. Therefore, the formation of $PrFeO_3$, which reduces the Pr content in (Ce, Pr)$O_{2-\delta}$, and/or difference in the firing temperature to obtain dense specimens are considered to be reasons for increase in the lattice constant as the volume fraction of $MnFe_2O_4$ increases.

The oxygen permeation and methane reforming properties were evaluated for the CPO-xMFO composites. A typical measurement result is shown in Fig. 4 for $Ce_{0.8}Pr_{0.2}O_{2-\delta}$ ($x = 0$) at 1000 °C. The oxygen flux density, jO_2, and selectivity were calculated from gas concentration as follows:

$$jO_2 = \left(\frac{[CO]}{2} + [CO_2]\right) \cdot f \cdot \frac{1}{60} \cdot \frac{1}{1000} \cdot \frac{1}{RT} \cdot \frac{1}{S} \quad (3)$$

$$\text{CO selectivity} = \frac{[CO]}{[CO] + [CO_2]} \times 100 \quad (4)$$

$$\text{H}_2\text{ selectivity} = \frac{[H_2]}{[H_2] + [H_2O]} \times 100 \quad (5)$$

where [CO], [CO_2], [H_2], and [H_2O] denote concentrations of the respective gases; f and S are a flow rate in sccm of Ar-10%CH_4 and cross-sectional area of specimen, respectively; R and T are gas constant and standard temperature, respectively. As can be seen in Fig. 4, the oxygen flux density as well as selectivity depends on a flow rate of Ar-10%CH_4. In general, the oxygen flux density tends to be higher as the flow rate increases. In the case of $Ce_{0.8}Pr_{0.2}O_{2-\delta}$, an oxygen flux density of 6 μmol·cm^{-2}·s^{-1} (L = 0.0247 cm) and the maximum methane conversion of 50% were attained at a flow rate of 20 sccm. The CO and H_2 selectivities higher than 95% were achieved for all specimens.

The oxygen permeability of CPO-xMFO composites under methane conversion atmosphere is plotted in Fig. 5(a) as a function of the volume fraction of $MnFe_2O_4$. The oxygen flux density was multiplied by a membrane thickness of L for comparison. As a reference, the oxygen permeability of CGO-xMFO composites is plotted in Fig. 5(b) in the same manner. In the case of CGO-xMFO (Fig. 5(b)), the oxygen permeability for the 1 vol% $MnFe_2O_4$ sample is limited to less than 1×10^{-8} mol·cm^{-1}·s^{-1} due to the lack of electronic conductivity; however, in the case of CPO-xMFO (Fig. 5(a)), the high oxygen permeability reaching to 1×10^{-7} mol·cm^{-1}·s^{-1} was observed even for $Ce_{0.8}Pr_{0.2}O_{2-\delta}$ without $MnFe_2O_4$. The high oxygen permeability found in CPO-xMFO regardless of the volume fraction of $MnFe_2O_4$ can be assigned to high mixed oxide-ion and electronic conductivity of Pr-doped CeO_2 itself. Shuk and Greenblat have reported an ionic transport number, t_{ion}, of $Ce_{1-x}Pr_xO_2$, where $0.05 \le x \le 0.30$. In the case of $x = 0.2$ and at 700 °C, t_{ion} was found to be 0.6 under a pO_2 gradient between 1.01×10^5 Pa and 0.21×10^5 Pa [11]. The mixed conductivity of $Ce_{1-x}Pr_xO_2$ was also confirmed by the pO_2 dependence of total conductivity by Stefanik and Tuller [10]. For CPO-xMFO, the small decrease in the oxygen permeability in the range of less than 5 vol% $MnFe_2O_4$ seems to be attributed to decrease in Pr content in the matrix ceria phase as a result of the formation of $PrFeO_3$ phase as mentioned above. At high $MnFe_2O_4$ level, the oxygen permeability increases with increasing $MnFe_2O_4$. This can be attributed to the establishment of percolation network of $MnFe_2O_4$ phase.

Arrhenius plots of oxygen permeability for samples with $x = 0$ and 15 are shown as an inset of Fig. 5(a). The activation energy of oxygen permeation was found to be 47 ± 1 and 54 ± 4 kJ/mol for the samples with $x = 0$ and 15, respectively. These values are close to those for $(Ce_{0.8}Gd_{0.2})_{2-\delta}$ − 15vol% $MnFe_2O_4$ (53 ± 1 kJ/mol). With respect to chemical and mechanical stabilities of CPO-xMFO during methane conversion, it was found that, for the samples with $x = 0$ to 3, their oxygen flux densities slightly decreased as time elapsed, and finally the samples were cracked presumably due to so-called "chemical expansion" originating from the reduction of Pr^{4+} and Ce^{4+} to 3+ states along with a large volume change. On the other hand, the samples with $x = 5$ to 25 were stable during methane conversion and no crack was

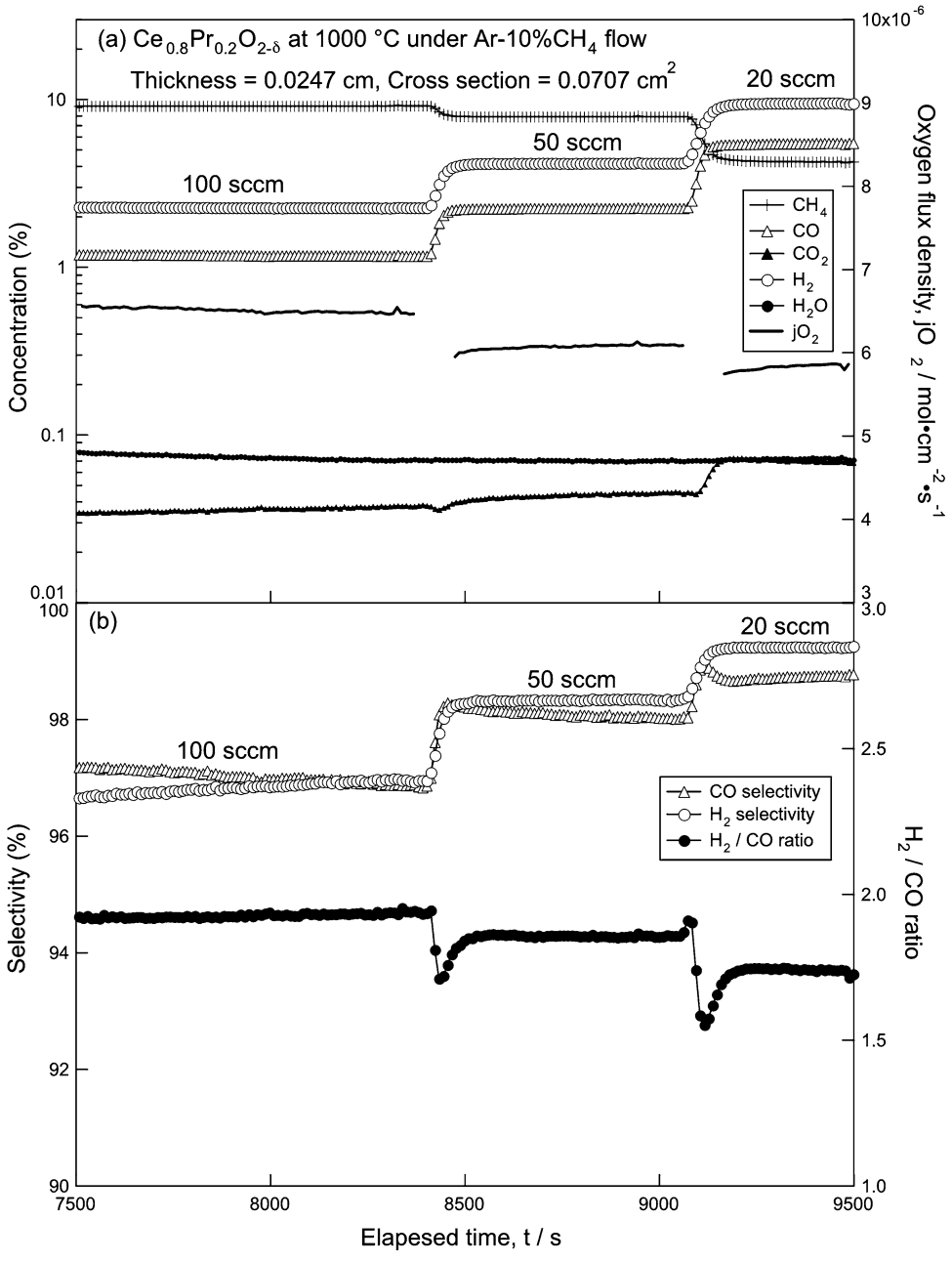

Fig. 4 The oxygen permeation and methane reforming properties of $Ce_{0.8}Pr_{0.2}O_{2-\delta}$ at 1000 °C under Ar-10%CH_4/air gas flow. The flow rate of Ar-10%CH_4 was varied from 100 to 20 sccm

found after measurements. This difference may suggests that, even though oxygen permeability seems to be comparable, an effective pO_2 gradient across a membrane strongly depends on the sample composition; the samples with a low volume fraction of $MnFe_2O_4$ may be highly reduced compared to those with a high volume fraction of $MnFe_2O_4$. In addition, the samples with x = 30 and 35 also showed a degradation of oxygen flux density and cracks after measurements. For high $MnFe_2O_4$ content, the degradation of samples is attributed to the instability of $MnFe_2O_4$ mentioned above. Therefore, to use the CPO-xMFO composites for methane conversion, the optimum volume fraction of $MnFe_2O_4$ appears to be 5 to 25.

3.2 Effects of FePt nanoparticles on oxygen permeation and fabrication of their Langmuir-Blodgett (LB) films

To improve the surface exchange kinetics of oxygen permeable ceramics, FePt nanoparticles were prepared and applied as a catalyst. The oxygen permeable ceramics used was the 0.3 mm-thick $(Ce_{0.8}Gd_{0.2})O_{2-\delta}$ − 15vol% $MnFe_2O_4$ (CGO-15MFO) composite. In our previous work, the oxygen flux density of the composite under a large pO_2 gradient caused by H_2/air gases was found to be almost constant in the case of membrane thickness, $L \leq 0.5$ mm [9]. The colloidal solution of FePt nanoparticles was dropped

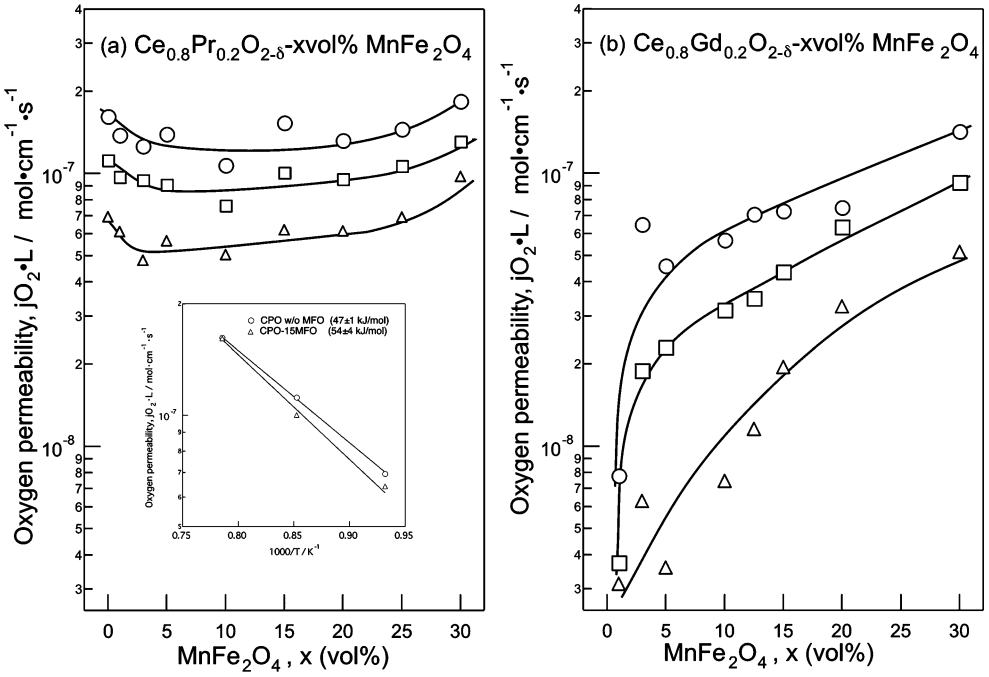

Fig. 5 The oxygen permeability, $jO_2 \times L$, of (a) $Ce_{0.8}Pr_{0.2}O_{2-\delta} - x$ vol% $MnFe_2O_4$ and (b) $Ce_{0.8}Gd_{0.2}O_{2-\delta} - x$ vol% $MnFe_2O_4$ as a function of the volume fraction of $MnFe_2O_4$; T = 800, 900, and 1000 °C

onto the diamond-polished surface of the sample to be a loading level of 2.8 mg/cm^2. The oxygen permeation properties of CGO-15MFO with the FePt nanoparticles at 1000°C were summarized in Table 2. Under small pO_2 gradients caused by He and air gas flow, the oxygen flux density was increased by a factor of 1.7 and 2.5 in the case of applying the catalyst on air-side surface and both surfaces, respectively. On the other hand, increase in the oxygen flux density was limited to 20% in the case of large pO_2 gradients caused by Ar-10%CH_4 and air gas flow. Even though morphological change of the FePt nanoparticles at elevated temperatures needs to be clarified, given that the loading level of the catalyst is only 2.8 mg/cm^2, FePt nanoparticles is considered to be a good catalyst for promoting the surface exchange kinetics of oxygen permeable membranes.

To precisely control the structure of the FePt nanoparticle catalyst layer, and to enlarge the region of surface modification, the Langmuir-Blodgett technique was applied. Figure 6 shows a π-A isotherm of FePt nanoparticles spread on a subphase of pure water. It demonstrates that the monolayer of FePt nanoparticles is stable at the air-liquid surface. The maximum surface pressure is reaching to 40 mN/m. Prior to the deposition on CGO-15MFO, LB films were prepared on a Si(100) wafer with a hydrophilic surface in order to analyze its structure by means of small-angle X-ray diffraction. The monolayer of FePt nanoparticles was transferred onto the Si wafer at a constant surface pressure of 25 mN/m. The deposition was repeated 29 times to obtain a 150 nm-thick LB film.

Figures 7(a) and (b) show the small-angle X-ray diffraction patterns of the LB film and self-assembled FePt nanoparticles as a reference, which was prepared by dropping the colloidal solution onto the same substrate followed by evaporation of solvent at room temperature. From the reflec-

Table 2 Oxygen flux density of $(Ce_{0.8}Gd_{0.2})O_{2-\delta} - 15$ vol% $MnFe_2O_4$ with FePt nanoparticles at 1000 °C.

	jO_2 (μmol·cm^{-2}·s^{-1}) He/air gradient	jO_2 (μmol·cm^{-2}·s^{-1}) Ar-10%CH_4/air gradient
w/o catalysts	0.30	5.0
Air-side surface	0.52	6.0
Both surfaces	0.76	6.0

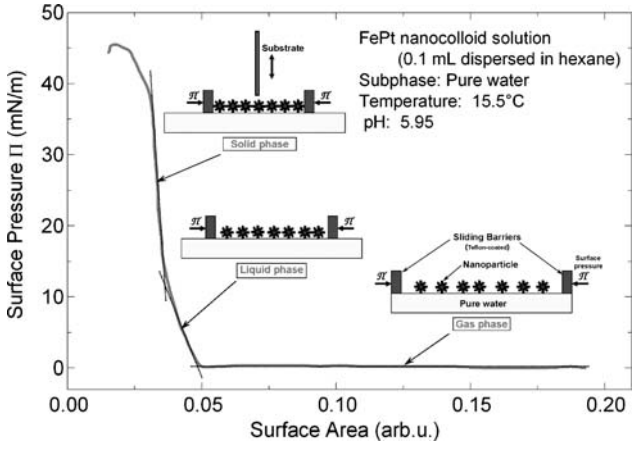

Fig. 6 The π-A isotherm of FePt nanoparticles spread onto a subphase of pure water (pH = 5.95) at 15.5 °C

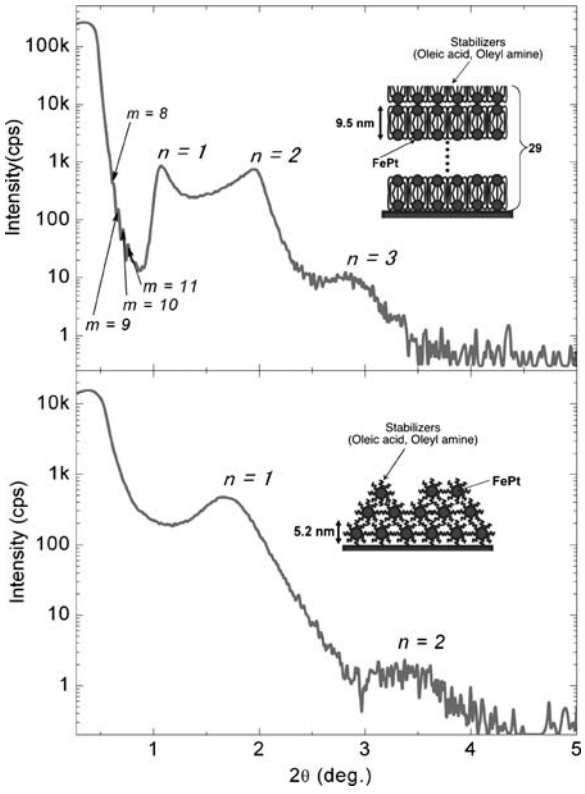

Fig. 7 Small-angle X-ray diffraction patterns of (a) the 150 nm-thick Langmuir-Blodgett film of FePt nanoparticles and (b) self-assembled FePt nanoparticles prepared by evaporation

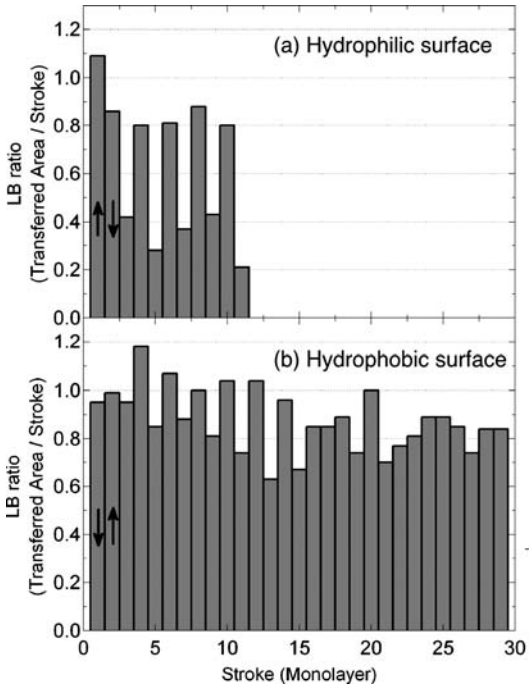

Fig. 8 The transfer ratio of the monolayer of FePt nanoparticles for the tape-cast $Ce_{0.8}Gd_{0.2}O_{2-\delta}$ − 15 vol% $MnFe_2O_4$ membrane after (a) hydrophilic or (b) hydrophobic treatments

tions in Fig. 7(b), in which the second order reflection ($n = 2$) was confirmed, the periodicity of self-assembled film was found to be 5.2 nm. This seems to correspond to a size of FePt nanoparticles including stabilizers as shown in the inset. On the other hand, judging from the presence of third order reflection ($n = 3$) in Fig. 7(a), the LB film appears to have a highly ordered structure. In addition, since interferences coming from a total film thickness (≈150 nm) which are denoted by $m = 1$ to 11 are observed, the homogeneity of the LB film thickness is superior compared to that for the self-assembled one. The periodicity of the LB film was found to be 9.5 nm, suggesting the presence of hydrophobic bonding of stabilizers to form FePt nanoparticle pairs as shown in the inset.

The LB films of FePt nanoparticles were then deposited on the CGO-15MFO membrane prepared by tape-casting. Figures 8(a) and (b) show the transfer ratio as a function of the number of stroke for the CGO-15MFO membrane with hydrophilic or hydrophobic surface, respectively. The deposition was carried out at a surface pressure of 15 mN/m and a dipping speed of 3 to 4 cm/min. As can be seen in Fig. 8(a), the transfer ratio tends to drastically decrease for downwards strokes in the case of the CGO-15MFO membrane with hydrophilic surface. In contrast, as shown in Fig. 8(b), high transfer ratio was achieved for the CGO-15MFO membrane with hydrophobic surface. Even though the transfer ratio slightly decreased with increasing the number of stroke, especially for downwards strokes, an average transfer ratio of 80% was achieved for hydrophobic surface. Figure 9 shows the SEM micrographs of (a) as hydrophobic-treated surface of the CGO-15MFO membrane, and (b) its surface after the deposition of the LB film. From Fig. 9(b), it is obvious that the surface of the CGO-15MFO membrane is homogeneously covered with the LB film of the FePt nanoparticles. While effects of the highly ordered LB film of FePt nanoparticles on the oxygen permeation properties as well as morphological change of the film at elevated temperatures are underway, this technique seems to be promising to fabricate a thin and uniform catalyst layer on oxygen permeable ceramics. It is also expected to be used for other applications such as an electrode for sensors and fuel cells.

4 Conclusions

The preparation and oxygen permeation properties of the $(Ce_{0.8}Pr_{0.2})O_{2-\delta}$ − xvol% $MnFe_2O_4$ composites, where $x =$ 0 to 35, have been investigated. In addition, the surface modification of the $(Ce_{0.8}Gd_{0.2})O_{2-\delta}$ − 15vol% $MnFe_2O_4$ composite was performed by combining FePt nanoparticles and the Langmuir-Blodgett technique.

For the $(Ce_{0.8}Pr_{0.2})O_{2-\delta}$ − x vol% $MnFe_2O_4$ composites, in addition to fluorite-type (Ce, Pr)$O_{2-\delta}$ and $MnFe_2O_4$ phases, $PrFeO_3$ was found to exist in the case of x ≥

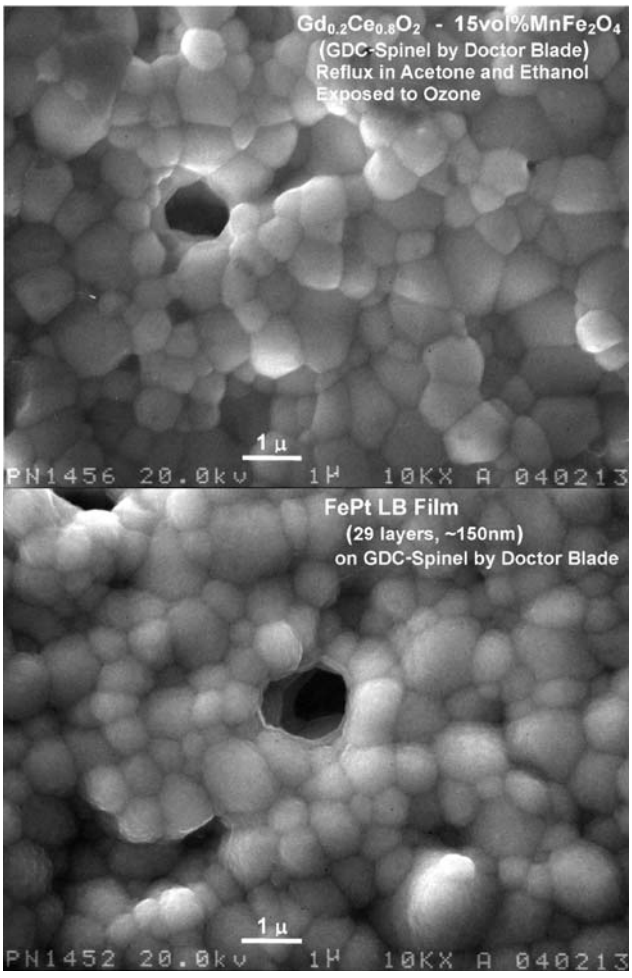

Fig. 9 SEM micrographs of (a) the tape-cast $Ce_{0.8}Pr_{0.2}O_{2\delta}$ − x vol% $MnFe_2O_4$ membrane after hydrophobic treatment and (b) its surface after the deposition of the 150 nm-thick Langmuir-Blodgett film of FePt nanoparticles

10 presumably due to the instability of $MnFe_2O_4$ under air. In the case of $Ce_{0.8}Pr_{0.2}O_{2-\delta}$, an oxygen flux density of 6 $\mu mol \cdot cm^{-2} \cdot s^{-1}$ (L = 0.0247 cm) and the maximum methane conversion of 50% were attained at 1000 °C under methane conversion atmosphere. Unlike the composites consisting of Gd-doped CeO_2 and $MnFe_2O_4$, the oxygen permeability of the $(Ce_{0.8}Pr_{0.2})O_{2-\delta}$ − x vol% $MnFe_2O_4$ composites is almost constant regardless of the volume fraction of $MnFe_2O_4$; however, the optimum volume fraction of $MnFe_2O_4$ was determined to be 5 to 25 in the context of the chemical and mechanical stabilities under methane conversion atmosphere.

The oxygen flux density of the $(Ce_{0.8}Gd_{0.2})O_{2-\delta}$ − 15 vol% $MnFe_2O_4$ composite was enhanced by applying the FePt nanoparticle catalyst layer. The catalyst loading of 2.8 mg/cm^2 on the both side of the 0.3 mm-thick $(Ce_{0.8}Gd_{0.2})O_{2-\delta}$ − 15 vol% $MnFe_2O_4$ composite increased the oxygen flux density from 0.30 to 0.76 $\mu mol \cdot cm^{-2} \cdot s^{-1}$ in the case of He / air gradients; however, the effect seems to be reduced in the case of high oxygen flux density caused by a large pO_2 gradient. The highly ordered Langmuir-Blodgett film of the FePt nanoparticles was successfully prepared on the tape-cast $(Ce_{0.8}Gd_{0.2})O_{2-\delta}$ − 15 vol% $MnFe_2O_4$ composite. Hydrophobic treatments on the surface of the composite were crucial to achieve high transfer ratio for the deposition of the LB film.

Acknowledgments This work has been supported in part by CREST of Japan Science and Technology Agency. HT is also grateful to Industrial Technology Research Grant Program in 2005 from New Energy and Industrial Technology Development Organization (NEDO) of Japan.

References

1. Y. Teraoka, H.M. Zhang, S. Furukawa, and N. Yamazoe, *Chemistry Letters*, 1743 (1985).
2. P.N. Dyer, R.E. Richards, S.L. Russek, and D.M. Taylor, *Solid State Ionics*, **134**, 21 (2000).
3. Z.P. Shao, G.X. Xiong, H. Dong, W.H. Yang, and L.W. Lin, *Separation and Purification Technology*, **25**, 97 (2001).
4. T. Ishihara, Y. Tsuruta, T. Todaka, H. Nishiguchi, and Y. Takita, *Solid State Ionics*, **152**, 709 (2002).
5. H. Takamura, K. Enomoto, Y. Aizumi, A. Kamegawa, and M. Okada, *Solid State Ionics*, **175**, 379 (2004).
6. V.V. Kharton, A.V. Kovalevsky, A.P. Viskup, F.M. Figueiredo, A.A. Yaremchenko, E.N. Naumovich, and F.M.B. Marques, *Journal of the European Ceramic Society*, **21**, 1763 (2001).
7. U. Nigge, H.D. Wiemhofer, E.W.J. Romer, H.J.M. Bouwmeester, and T.R. Schulte, *Solid State Ionics*, **146**, 163 (2002).
8. H. Takamura, M. Kawai, K. Okumura, A. Kamegawa, and M. Okada, in *Preparation and Oxygen Permeability of Gd-Doped Ceria and Spinel-Type Ferrite Composites* (Materials Research Society, Boston, USA, 2002), pp. EE8.11.1.
9. H. Takamura, K. Okumura, Y. Koshino, A. Kamegawa, and M. Okada, *Journal of Electroceramics*, **13**, 613 (2004).
10. T.S. Stefanik and H.L. Tuller, *Journal of Electroceramics*, **13**, 799 (2004).
11. P. Shuk and M. Greenblatt, *Solid State Ionics*, **116**, 217 (1999).
12. D.P. Fagg, V.V. Kharton, A. Shaula, I.P. Marozau, and J.R. Frade, *Solid State Ionics*, **176**, 1723 (2005).
13. H. Takamura and H.L. Tuller, *Solid State Ionics*, **134**, 67 (2000).
14. H. Takamura, K. Enomoto, A. Kamegawa, and M. Okada, *Solid State Ionics*, **154**, 581 (2002).
15. C. Kleinlogel and L.J. Gauckler, *Solid State Ionics*, **135**, 567 (2000).
16. S.H. Sun, C.B. Murray, D. Weller, L. Folks, and A. Moser, *Science*, **287**, 1989 (2000).
17. H. Takamura, T. Kobayashi, T. Kasahara, A. Kamegawa, and M. Okada, *Journal of Alloys and Compounds*, **408–412**, 1084 (2006).
18. H.I. Yoo and H.L. Tuller, *Journal of Materials Research*, **3**, 552 (1988).
19. G. Bonsdorf, K. Schafer, K. Teske, H. Langbein, and H. Ullmann, *Solid State Ionics*, **110**, 73 (1998).
20. Y. Takasu, T. Sugino, and Y. Matsuda, *Journal of Applied Electrochemistry*, **14**, 79 (1984).
21. M. Nauer, C. Ftikos, and B.C. H. Steele, *Journal of the European Ceramic Society*, **14**, 493 (1994).
22. A.E. Sovestnov, V.A. Shaburov, B.T. Melekh, I.A. Smirnov, Y.P. Smirnov, A.V. Tyunis, and A. I. *Egorov, Fizika Tverdogo Tela*, **36**, 1140 (1994).